Correspondence to:
E. Guiltinan,
Eric.Guiltinan@lanl.gov

Two-Phase Fluid Flow Properties of Rough Fractures With Heterogeneous Wettability: Analysis With Lattice Boltzmann Simulations

Eric J. Guiltinan[1] , J. E. Santos[2] , M. Bayani Cardenas[3] , D. Nicolas Espinoza[2] , and Qinjun Kang[1]

[1]Computational Earth Science, Los Alamos National Lab, Los Alamos, NM, USA, [2]Hildebrand Department of Petroleum and Geosystems Engineering, The University of Texas at Austin, Austin, TX, USA, [3]Department of Geological Sciences, The University of Texas at Austin, Austin, TX, USA

Abstract Fractures are conduits for fluid flow in low-permeability geological formations. Multiphase flow properties of fractures are important in natural processes and in engineering applications such as the evaluation of the sealing capacity of caprocks and productivity of hydrocarbon-bearing tight rocks. Investigations of flow and transport through fractures typically focus on the effects of fracture geometric and mechanical factors such as aperture, roughness, and compressibility. The wettability of the fracture surfaces and its influence on microscale interfacial phenomena and macroscale effective transport properties are seldom studied. Here, we investigated the effect of heterogeneous wetting properties on the displacement of water by supercritical CO_2 through a series of lattice Boltzmann method simulations. The results show the evolution of the CO_2 plume within a fracture is controlled by both the roughness of the aperture field and the wetting distribution. We combined these factors into a capillary pressure map that can be related to the macroscopic flow behavior of the fracture. We observed that heterogeneous wetting distributions promote the residual trapping of water where lower capillary pressures allowed for isolated water pockets in higher capillary pressure zones. Analysis of fracture unsteady relative permeability shows the effect of wetting on permeability evolution and provides support for the viscous-coupling relative permeability model. Finally, analysis of the steady-state relative permeability and saturation demonstrates a strong correlation between permeability and the standard deviation of the capillary pressure field. Thus, characterizing the distribution of wetting properties of fractures is crucial to understanding multiphase fracture flow and transport properties.

1. Introduction

The geologic storage of CO_2 is a viable option for the reduction of CO_2 emissions into the atmosphere (Pacala & Socolow, 2004). The process involves capturing CO_2 at large emission points and injecting it into underground reservoirs. Once underground, CO_2 rises buoyantly until trapped beneath a low-permeability caprock such as an evaporite or shale (Benson et al., 2005). However, some of these formations, particularly brittle shales, may have high permeability fractures that reduce their trapping capacity. Predicting the transport of CO_2 through fractures is critical for ensuring safe CO_2 storage, and quantifying potential leak rates.

The flow of two immiscible fluids through a fracture is controlled by the fracture geometry, fluid properties, pressure gradient, and the fluid-solid interfacial properties (wettability) (Guiltinan et al., 2017; Renshaw, 1995; Vogler et al., 2018; Wang & Cardenas, 2014; Wang et al., 2015). Except for wettability, each of these properties have been studied in-depth. In porous media, it has long been understood that wettability impacts residual saturation and relative permeability. However, the effects of surface wetting properties in fractures remain relatively unexplored due to the difficulty in conducting controlled fracture experiments and running computationally challenging 3D fracture models.

The pore-scale controls on transport processes involving two-phase, immiscible flow have been well studied through physical and numerical simulation experiments (Al-Raoush, 2009; Armstrong et al., 2012; Blunt et al., 2013; Chaudhary et al., 2013; Culligan et al., 2006; Dou et al., 2013; Hao & Cheng, 2010; Hu et al., 2017). Generally, investigating pore-scale systems using computational models requires solving the Navier-Stokes equations. This is computationally expensive however and it can be difficult for traditional

modeling methods to incorporate the intermolecular forces responsible for surface phenomena such as wettability, solubility, phase separation, and capillary pressure (Chen & Doolen, 1998; Coon et al., 2014). The lattice Boltzmann method allows for the inclusion of these forces in a simple manner while also approximating the Navier-Stokes equations solution (Aidun & Clausen, 2010; Chen & Doolen, 1998; Chen et al., 2014; Li et al., 2016; Nourgaliev et al., 2003; Zhang, 2011); it is thus a promising and advantageous method for modeling-based investigation of pore-scale multiphase flow.

The lattice Boltzmann method (LBM) is based upon tracking a distribution of particles, $f_i(\mathbf{x}, t)$, moving upon a grid as they relax toward an equilibrium Maxwell-Boltzmann distribution f_i^{eq}. Intermolecular forces, both between fluids and walls, can be incorporated through the application of an attractive or repulsive force on the particles (Chen & Doolen, 1998). In this way, the LBM interparticle forces represent a more natural expression of intermolecular forces than traditional computational fluid dynamics techniques, such as the volume-of-fluid method and fluid-fluid interface tracking/capturing (Meakin & Tartakovsky, 2009). A recent study explored the effect of wettability heterogeneity on relative permeability of immiscible flow in porous media using LBM (Zhao et al., 2018). The results show that for moderate water saturations (between 0.3 and 0.7) the relative permeability of random wetting distributions was less than that of purely water-wet or purely nonwater-wet, but that this trend reversed at very high or low saturations. However, these results are in a 2D homogeneous regular structure with porosity of 75% and may not be suitable for 3D porous media.

The LBM has also been used to investigate fractures (Dou et al., 2013; Eker & Akin, 2006; Ju et al., 2017; Kim et al., 2003; Landry et al., 2014; Santos et al., 2018). Landry et al. (2014) showed that the LBM was able to accurately reproduce the matrix fluid transfer in an oil-wet and water-wet sintered glass fracture as visualized with X-ray computed microtomography. However, they were not able to reproduce the irreducible water saturation and hypothesized that a significantly finer resolution may be needed. Dou et al. (2013) investigated the effect of altering the magnitude of wetting in a homogeneously wet self-affine fracture and simulating displacement by incremental pressure. Due to the homogeneous wetting conditions of their fracture simulations the flow field in each fracture was similar but the wettability magnitude had a significant effect on the evolution of effective interfacial area in time. These studies reveal the potential importance of wetting on flow in fractures but do not study realistic heterogeneous distributions.

The unsteady nature of the fluid displacement process within a fracture is a challenge for experiments as well as modeling efforts. During multiphase flooding in the field, either for CO_2 sequestration, enhanced oil recovery, geothermal energy, or some other application, steady-state flow is achieved only when all the injected fluid is also produced. Therefore, relative permeability curves, which are commonly constructed at steady-state saturations, lack the information necessary to describe the transient displacement process. During oil production, the Jonson, Bossler, and Naumann (JBN) method or a variant is typically used on production data (Johnson et al., 1959; Ramstad et al., 2012). This method assumes that the flow velocity is high enough so that capillary pressure can be disregarded and unsteady permeability can be calculated from the production data and pressure drop. Laboratory experiments which minimize capillary effects by using loose sandpacks and impose gravity drainage have had success in developing relative permeability curves from unsteady saturation experiments (Dehghanpour et al., 2011; DiCarlo et al., 2000; Kianinejad et al., 2016; Naylor et al., 1996; Sahni et al., 1998). However, in reality capillary, effects may be significant during multiphase flow. Experiments, which take into account capillary effects during unsteady displacement, are difficult but can been performed (Chen et al., 2017; Zhao et al., 2019). While numerical simulations, such as with the LBM, hold promise to investigate their full range of effect on the evolution of permeability with time.

In this study, we investigate the effect of nonuniform wettability distributions on $scCO_2$ flow in fractures through the use of the "explicit-forcing" multicomponent Shan and Chen model (Porter et al., 2012; Shan & Chen, 1993, 1994). We apply wetting parameters on fracture walls informed by real-shale mineral distributions to a set of synthetic fractures with varying aperture roughness and mean aperture. The ultimate goal of this work is to determine the effect of heterogeneous wetting distributions on multiphase displacement in realistic fractures. We quantify this process through an analysis of the evolution of unsteady relative permeability, breakthrough time, and residual saturation.
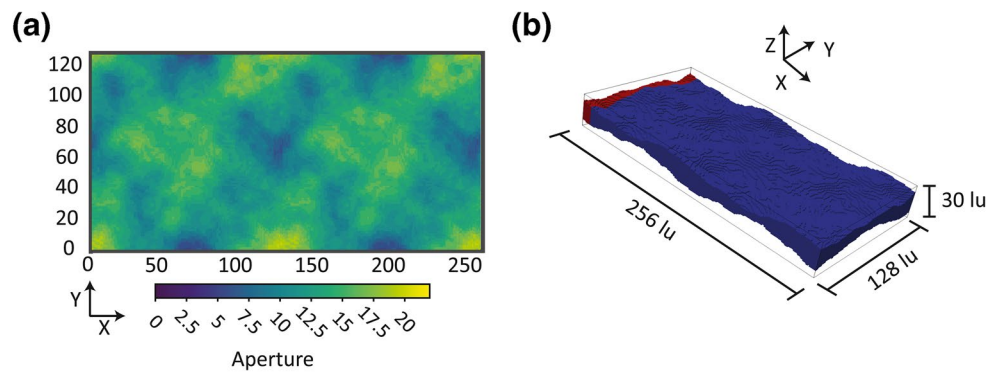
Figure 1. a) Aperture field of fracture with fractal dimension 1.75 and mean aperture 12.7. The aperture ranges from 5 to 20 lu with an average aperture opening of 12.7 lu. (b) Model domain. The model domain is $256 \times 128 \times 30$ lu with a constant pressure inlet at $x = 0$ and a lower constant pressure outlet at $x = 256$. scCO$_2$ (red) is initialized in the first 10 lu in the x-direction while the remaining model is brine (blue).

2. Methods

2.1. Lattice Boltzmann Method and the *Taxila* Code

To effectively simulate variable wetting properties and the high viscosity ratio of supercritical scCO$_2$ and water we use the *Taxila* LBM simulator, an open source code developed at Los Alamos National Laboratory (Coon et al., 2014; Porter et al., 2012) (https://github.com/ecoon/Taxila-LBM). *Taxila* implements the multicomponent interparticle-potential model known as the Shan-Chen (SC) model (Shan & Chen, 1993, 1994) with several enhancements as outlined in Porter et al. (2012) and Yu et al. (2011). These enhancements have addressed some drawbacks of the original SC model such as large spurious currents near interfaces, viscosity-dependent equilibrium densities, and numerical instabilities for large kinematic viscosity ratios.

In this study, we use the multiple relaxation time version of the three-dimensional D3Q19 model and enforce eight orders of isotropy. The D3Q19 model represents a three-dimensional mesh with 18 velocities leaving each node plus one stationary "velocity" which represents no movement. Variable wettability (contact angle) is achieved by changing the strength of the intermolecular force between each fluid phase and mineral. More details regarding *Taxila* are available elsewhere (Coon et al., 2014; Porter et al., 2012).

2.2. Synthetic Fracture Generation and Model Geometry

To generate realistic fracture surfaces upon which to drape our wetting parameters, we use SynFrac, a program developed to create synthetic fractures based on natural analogs (Ogilvie et al., 2006). Four fractures with 128×128 lattice units (lu) were created using the Glover method with a standard deviation of 2.5, a mismatch length of 30 (lu), and a fractal dimension of 1.5, 1.75, 2.0 and 2.25 respectively (Glover et al., 1998a, 1998b). The fractures become rougher as the fractal dimension increases. A mismatch of 30 lu was selected as it created a fracture with noticeable differences between the top and bottom fracture walls. The geometry was repeated once in the x-direction to create fractures that were 256×128 lu. We normalized the mean aperture of all our fractures to have a fixed value of 12.7 lu. Each of the four fractures was then decreased by 3 lu to create a set of fractures with a mean aperture of 9.7 lu and increased by three voxels to create a set of fractures with a mean aperture of 15.7 lu. The final result is four fractures with increasing roughness with three different mean apertures for a total of 12 fractures (Figure 1a).

We assume the average aperture of 12.7 lu corresponds to a fracture opening of 50 μm since fractures hosting apertures of 50 μm are commonly observed in the Barnett formation (Gale et al., 2007); this results in a resolution (dx) of 3.94 μm/lu. The LBM assumes incompressible flow in order to recover the Navier-Stokes equations solution. This assumption is only valid when the lattice velocity is significantly less than the speed of sound on the lattice, i.e., low Mach number conditions (Sukop & Thorne, 2006). To remain in the incompressible regime, we assume the convention of $dt/dx = 0.01$ which results in a time step of 3.94×10^{-8} s. We
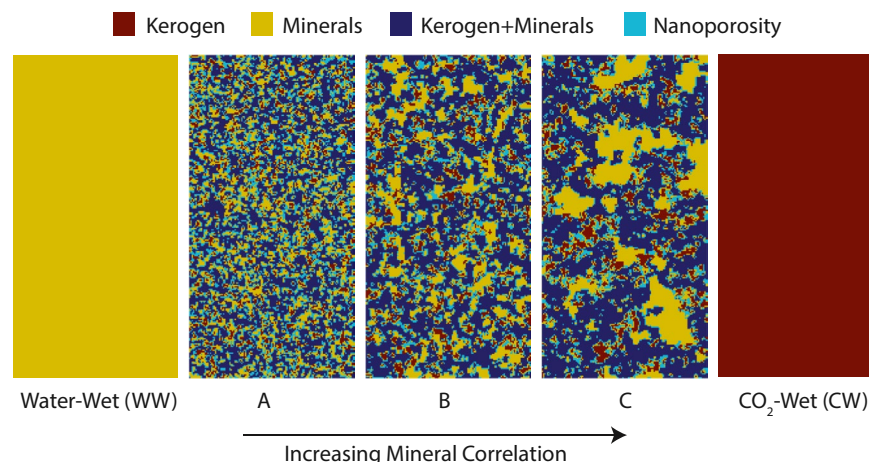
Figure 2. Five different wetting distributions applied to the fracture walls. Colors represent different phases: red—kerogen, yellow—minerals, dark blue—mixture of kerogen and minerals, light blue-nanoporosity.

use dt and dx to convert our units to physical properties by matching the dimensionless parameters; and our results could also be scaled to fractures of different apertures.

The model domain is $256 \times 128 \times 30$ lu and is initialized with scCO$_2$ present in the first 10 columns along the x axis while water defends in the remaining fracture volume (Figure 1b). The final 6 rows ($x = 251$–256) are repeated to improve numerical stability. Supercritical CO$_2$ invades the fracture at a constant pressure inlet located at $x = 0$. For calculating saturation and permeability, we treat $x = 250$, the last row which is not repeated, as the outlet. We set each the bulk density of both phases to be unity and the inlet pressure in lattice units is 0.38 and the outlet is 0.33, which corresponds to a differential pressure of 500 Pa in physical units. The constant pressure boundary condition implementation in *Taxila* is modified at the outlet to enforce a constant pressure in the water phase at $x = 256$. The effect of this modification is that there is a thin layer of water at the boundary which the scCO$_2$ is continuously attempting to displace. The scCO$_2$ is removed as it reaches $x = 256$. This avoids the capillary end effects that would occur if the scCO$_2$ was allowed to equilibrate to the prescribed outlet pressure. The model is periodic in the y-direction.

2.3. Heterogeneous Wettability Distributions

Wettability distributions are informed by mapped mineral distributions in an organic shale sample presented as images in Gerke et al. (2015). Gerke et al. (2015) developed a method for fuzing multiscale images obtained from X-ray microtomography and scanning electron microscopy into one image. They demonstrated their technique on an organic shale from the Bazhenov formation in Siberia where they created an
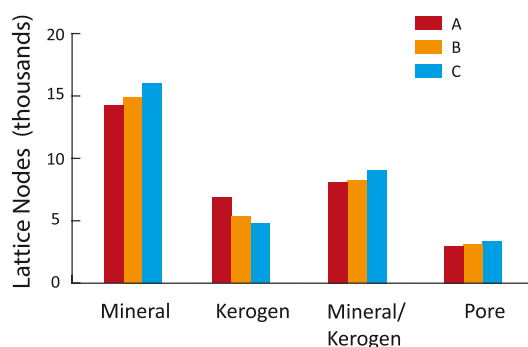

Figure 3. Histogram of the mineral components in each wetting distribution.

image with four distinct components: macroscale minerals, a mixture of minerals and kerogen, resolved kerogen, and kerogen nanoporosity. We subsampled their image (Gerke et al., 2015; Figure SI.7c) into a 744×372 image and created three new images using the Stanford Geostatistical Modeling Software (SGeMS, Remy et al., 2009). Each image was created by using the original image as training set with the "single normal equation simulation" algorithm and either 1, 3, or 5 multigrids. The use of increasing grids better represents larger structures (Remy et al., 2009). Each image contains similar histograms but different mineral distributions (Figures 2 and 3). The apparent clustering of the minerals (yellow phase) increases from mineral distribution A to C, with the C image being the most clustered. These distributions are draped onto the fracture walls in our model. Along with the three heterogeneous wetting distributions, we also explore the effect of a completely nonwetting and a completely wetting case. Sixty unique fractures were created from three fracture ap-
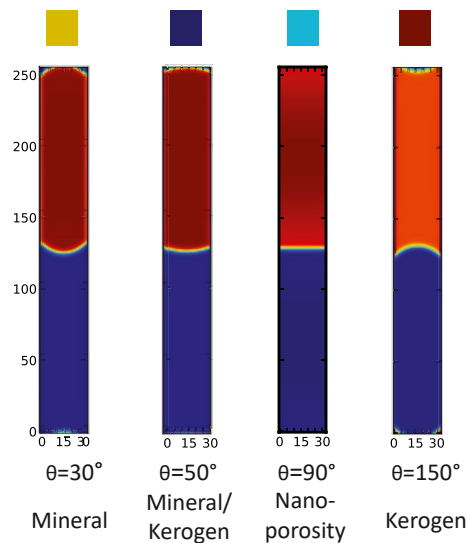
Figure 4. Contact angles of water for each mineral measured through the water phase (blue).

ertures (thin "T," regular "R," and wide "W") combined with four fractal dimensions (1.5, 1.75, 2.0, and 2.25) and five wetting distributions [sc-CO_2-wet (CW), A, B, C, water-wet (WW)]. Thus, fracture R-1.75-CW represents a fracture with a mean aperture of 12.7 lu, a fractal dimension of 1.75, and is scCO_2-wet (Table 1).

2.4. Parameter Determination and Model Verification

The lattice wettability force, g_k^m, between water and each mineral pair in our model is −0.145 for minerals (highly water-wet), −0.0675 for minerals and kerogen (moderately water-wet), 0 for kerogen nanoporosity (no wettability force), and 0.145 for kerogen (highly scCO_2 wet). The values are reversed for scCO_2. The resultant static contact angles due to these forces are measured from capillary models (Figure 4). These forces are meant to represent general wetting and nonwetting conditions which may be observed in the subsurface. The dynamic contact angle within our simulations will vary depending on local conditions, such as the local capillary number, roughness, and the applied forces. The interparticle force, $g_{k,\bar{k}}$, is set to 0.21. This value was found to maximize immiscibility while maintaining numerical stability. The explicit-forcing model has been shown to reproduce the Laplace equation (Porter et al., 2012) and so the pressure differential inside and outside of a bubble was used to calculate the interfacial tension. Under these conditions, the interfacial tension is 0.093 in lattice units. Liu et al. (2011) report Mt. Simon sandstone conditions, a potential location for CO_2 storage, to be 75 °C and 2,900 psi. At this condition CO_2 is supercritical and has an approximate dynamic viscosity of 5×10^{-5} poise and an approximate density of 600 kg/m^3 (Lemmon et al., 2020). Using these values and a dynamic viscosity of water of 1×10^{-3} and density of 1,000 kg/m^3, we calculate the kinematic viscosity ratio to be ~12-1 (1.0×10^{-6} m^2/s water/8.33×10^{-8} m^2/s CO_2). To achieve this ratio, the relaxation time was set to 3.5 (water) and 0.75 (scCO_2); this corresponds to kinematic viscosities of 1 lu (water) and 0.0833 lu (scCO_2). The capillary number ($Ca = \dfrac{\mu V}{\sigma}$) is calculated using the interfacial tension, the viscosity of scCO_2 and the average velocity at steady state for each model and ranges from a minimum of 5×10^{-3} in T-2.25-WW to a maximum of 1.2×10^{-2} in W-1.5-CW. Fluid flows at capillary numbers below ~1×10^{-4} are dominated by surface forces such as the wettability of the surface and interfacial tension of the fluids (Peters, 2012). The capillary number of our simulations can be considered a transitional capillary number, i.e., the flow is influenced by both viscous and surface forces.

The capillary pressure P_c between parallel plates is described by the Young-Laplace equation (Laplace, 1799; Young, 1805):

$$P_c = \frac{2\sigma \cos(\theta)}{a} \tag{1}$$

where θ is the contact angle of water, σ is the interfacial tension between the water and scCO_2, and a is the fracture aperture. Capillary pressure maps can be created for each fracture and wetting distribution combination by calculating the capillary pressure at each voxel (Figure 5). This novel concept combines the effect of the fracture aperture and the wettability of the minerals into a single continuous field.

Variograms of the capillary pressure fields are modeled using SGeMS. The range of the variance, which describes the correlation of the field, is shown to increase from A to C (Figure 6). Recently, An et al. (2020) showed that for porous media applications the correlation length of the pore size distribution should be 1/20th of the minimum sample dimension to guarantee an REV. While we do not attempt to define an REV of a single fracture here, we want to ensure to that our simulations are not sensitive to different realizations of the wetting patterns. Considering our capillary pressure field as generally representative of a pore size distribution within a porous media we can apply this 1/20th requirement. Our largest correlation length of the capillary pressure field is for wetting distribution C which is 7.4 lu. In the *y*-direction, our sample is

Table 1
Fracture Designations for All 60 Fractures

T-1.5-CW	T-1.75-CW	T-2.0-CW	T-2.25-CW	R-1.5-CW	R-1.75-CW	R-2.0-CW	R-2.25-CW	W-1.5-CW	W-1.75-CW	W-2.0-CW	W-2.25-CW
T-1.5-A	T-1.75-A	T-2.0-A	T-2.25-A	R-1.5-A	R-1.75-A	R-2.0-A	R-2.25-A	W-1.5-A	W-1.75-A	W-2.0-A	W-2.25-A
T-1.5-B	T-1.75-B	T-2.0-B	T-2.25-B	R-1.5-B	R-1.75-B	R-2.0-B	R-2.25-B	W-1.5-B	W-1.75-B	W-2.0-B	W-2.25-B
T-1.5-C	T-1.75-C	T-2.0-C	T-2.25-C	R-1.5-C	R-1.75-C	R-2.0-C	R-2.25-C	W-1.5-C	W-1.75-C	W-2.0-C	W-2.25-C
T-1.5-WW	T-1.75-WW	T-2.0-WW	T-2.25-WW	R-1.5-WW	R-1.75-WW	R-2.0-WW	R-2.25-WW	W-1.5-WW	W-1.75-WW	W-2.0-WW	W-2.25-WW

Three fracture apertures: thin "T," regular "R," and wide "W" combine with four fractal dimensions (1.5, 1.75, 2.0, and 2.25) and five wetting distributions CO_2-wet, A, B, C, and water-wet to create 60 unique fractures.

35 times this correlation length and 17 times this correlation length in the *x*-direction. While this a little less than the suggested size in the *x*-dimension, this boundary is periodic and the size of the x-dimension exceeds 1/20th requirement for the other wetting distributions.

The LBM is a finite difference scheme and thus the resolution of the model can impact the accuracy of the flow field. Given sufficiently large apertures, the LBM has been shown to accurately reproduce the analytical solution for single phase flow between parallel plates, an analog for fractures (Ju et al., 2017; Kim et al., 2003). However, our fractures with lattice nodes as narrow as 0 lu (contact points) are designed to mimic real world fractures. We conducted a series of two-dimensional parallel plate models using the same model parameters as our larger 3D fracture in order to investigate the accuracy of the *Taxila* LBM code in areas where the aperture becomes very small (Figure 7). The parallel plate models range from a fracture width of 1–6 lu. Resolution errors increase as the aperture decreases but remaininaccurate at small apertures. The area of the fractures that are composed of apertures <4 lu is small. Thin fracture #4 has the largest amount of patches of <4 lu; however by volume, they represent only 0.4% of the fracture and, therefore, these errors are assumed to be negligible.

The simulations were performed on the "Grizzly" high-performance computing cluster at Los Alamos National Lab. In general, each simulation was performed using 3,600 cores and reached steady state within 90 min for a total of ~324,000 CPU-hours for the 60 simulations.

3. Results and Discussion

Supercritical CO_2 displacing water was simulated in each of the three fracture apertures (thin to wide), four fractal dimensions (smooth to rough), and five wetting distributions (water-wet, A, B, C, $scCO_2$-wet). The results and discussion have been divided into four sections. First, we present the evolution of the $scCO_2$ plume during immiscible displacement as roughness and capillary pressure correlation are increased. We examine breakthrough time and breakthrough saturation as a surrogate to describe the behavior of the plume and we
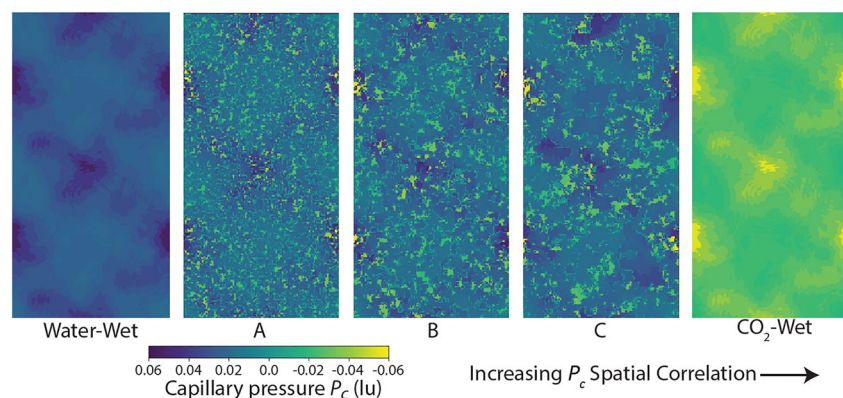

Figure 5. Capillary pressure maps created by mapping the mineral distributions from Figure 2 onto fracture R-1.75 (Figure 1) and applying Equation 1.
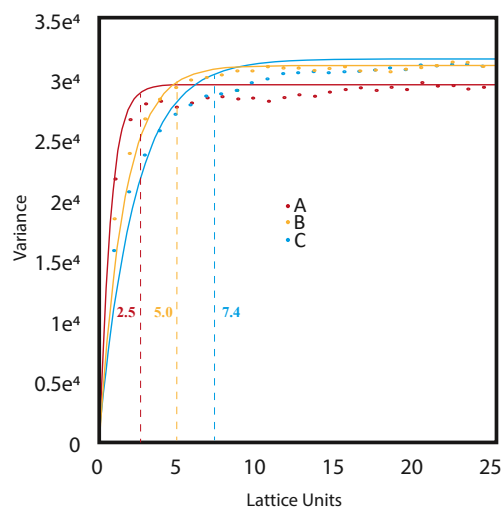
Figure 6. Variograms of the capillary pressure of each wetting distribution. The range of the variance of wetting distributions A, B, and C are ~2.5, 5.0, and 7.4 lu, respectively.

also describe two observed trapping mechanisms. Second, we present the results from an analysis of the unsteady permeability during our simulations and, third, we compare our unsteady permeability analysis to commonly used relative permeability models for fractures. Finally, we present the final residual saturation and final steady-state relative permeability of each of our simulations and show a strong correlation to the standard deviation of the capillary pressure field.

3.1. scCO$_2$ Plume Evolution and Residual Trapping

The scCO$_2$ plume evolution within the fracture is controlled by both the roughness of the fracture aperture and the wettability distribution. Figure 8 presents a series of snapshots from the regular aperture water-wet fractures at each fractal dimension where the upper surface of the fracture is primarily in view. As the fractal dimension is increased the fractures become rougher and more water is residually trapped on the fracture surfaces.

Figure 9 presents evolution of scCO$_2$ plume during each regular aperture with fractal dimension of 2.0, and Figure 10 presents the breakthrough time and corresponding average scCO$_2$ saturation for each wetting distribution across all fractures. The breakthrough time and saturation provide a snapshot of the plume behavior. Breakthrough saturation represents the degree to which the displacing fluid has fingered with low saturations representing more fingering and breakthrough time represents the rate at which the displacement has happened. The completely scCO$_2$ wetting and completely water-wetting cases bound the behavior of the system with the heterogeneous wetting cases falling in between. In general, as capillary pressure correlation is increased from A to C, time to breakthrough is decreased and the water sweep efficiency by scCO$_2$ is reduced. However, the completely scCO2 wetting case corresponds to both the highest breakthrough scCO$_2$ saturation and the shortest breakthrough time, and the completely water-wetting case is the opposite.

Trapping mechanisms during immiscible displacement in fractures have been studied at very low capillary numbers through an iterative process of slowly increasing the inlet pressure during LBM simulations with constant wetting parameters (Dou et al., 2013) and through the use of invasion percolation models (Yang et al., 2016). Here, we report the first analysis of trapping mechanisms during immiscible displacement of fractures with nonnegligible viscous forces, heterogeneous wetting, and varied apertures. Two mechanisms are observed in the trapping of residual water pockets. The first trapping mechanism is the most prevalent and is the formation of water films along the surface of the fracture. This happens when scCO$_2$ avoids water-wetting portions of the fracture surface through the central portion of the fracture (Figure 11a). These water films exist on the upper and lower surfaces of the fracture with scCO$_2$ occupying the center of the fracture. In this way, the effective aperture available to scCO$_2$ flow is decreased. This mechanism is increased as fracture roughness and aperture increase. Roughness within water-wetting surfaces provides locations for trapped films to exist while an increase in aperture reduces velocities and provides space for the water films to develop.

The second trapping mechanism observed is the enveloping of water by scCO$_2$. This occurs when an area of low capillary pressure allows the scCO$_2$ to completely surround water within a higher capillary pressure zone. This is most commonly observed in the narrow fractures with wetting distributions "B" and "C." The higher correlated capillary pressures mean that larger zones of high and low capillary pressures exist within the fracture. These larger zones promote the isolation of water pockets
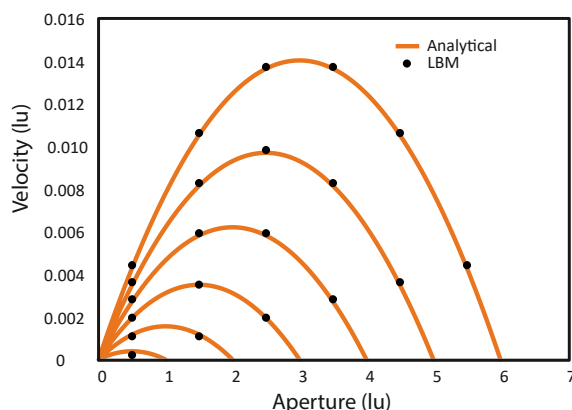

Figure 7. Comparison between simulations of flow between parallel plates and the analytical solution.
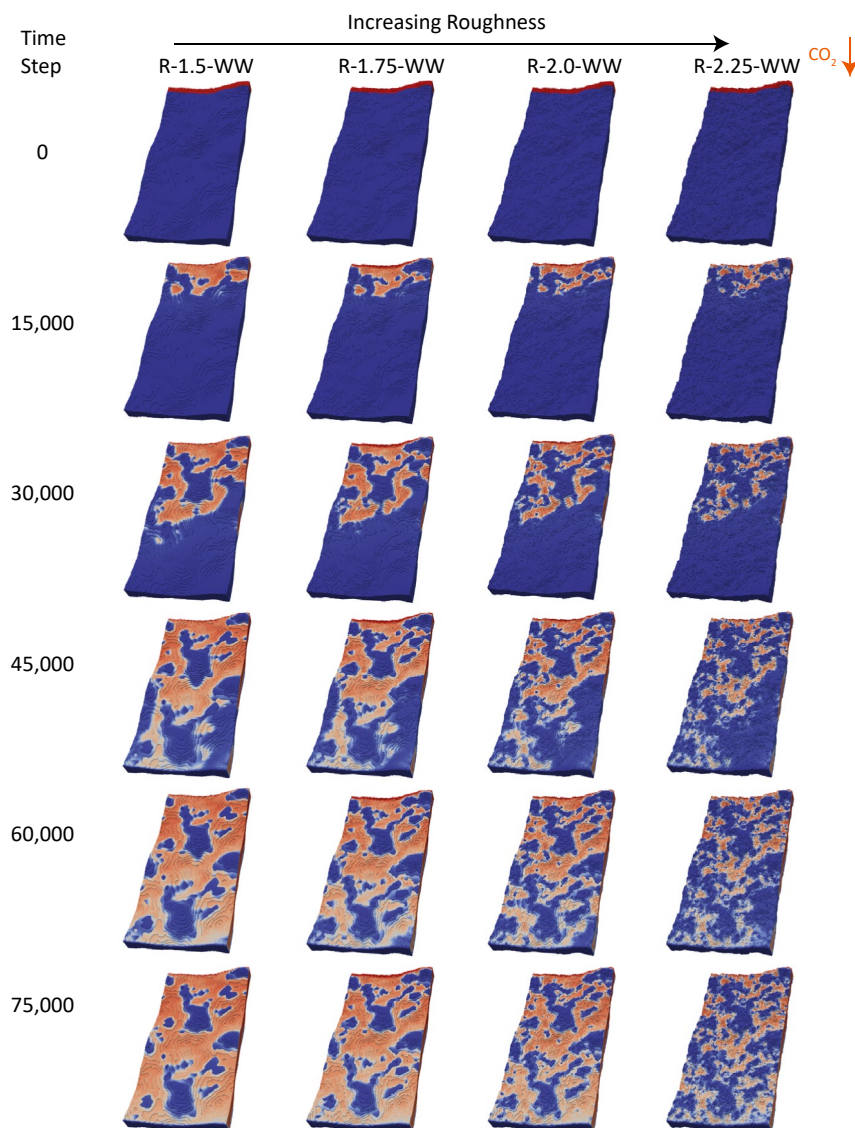
Figure 8. Evolution of CO_2 plume during each regular aperture, water-wetting simulation. As the fracture becomes rougher more water is trapped and the final $scCO_2$ saturation is decreased.

as $scCO_2$ bypasses the high capillary pressure zones. This mechanism is less prevalent in wetting case "A," as well as the completely water-wet fracture. This mechanism fully traps water droplets that exist from the upper surface to the lower surface of the fracture leaving a zone of the fracture unavailable for $scCO_2$ flow (Figure 11b).

3.2. Unsteady Displacement

Another way to study the evolution of the plume during the displacement process is through the analysis of the unsteady relative permeability. During CO_2 flooding, at steady state the injected CO_2 volume is equal to the extracted CO_2 and no water is produced. While relative permeability is typically measured at steady state, in reality, it is the evolution of relative permeability that is important for many applications. Measuring unsteady relative permeability is an instantaneous process, where the pressure drop (dp), and associated length (dl), are transient. At high capillary numbers and in homogeneous medium, surface forces can be assumed negligible and a sharp front can be formed (Buckley & Leverett, 1942). Measuring unsteady relative
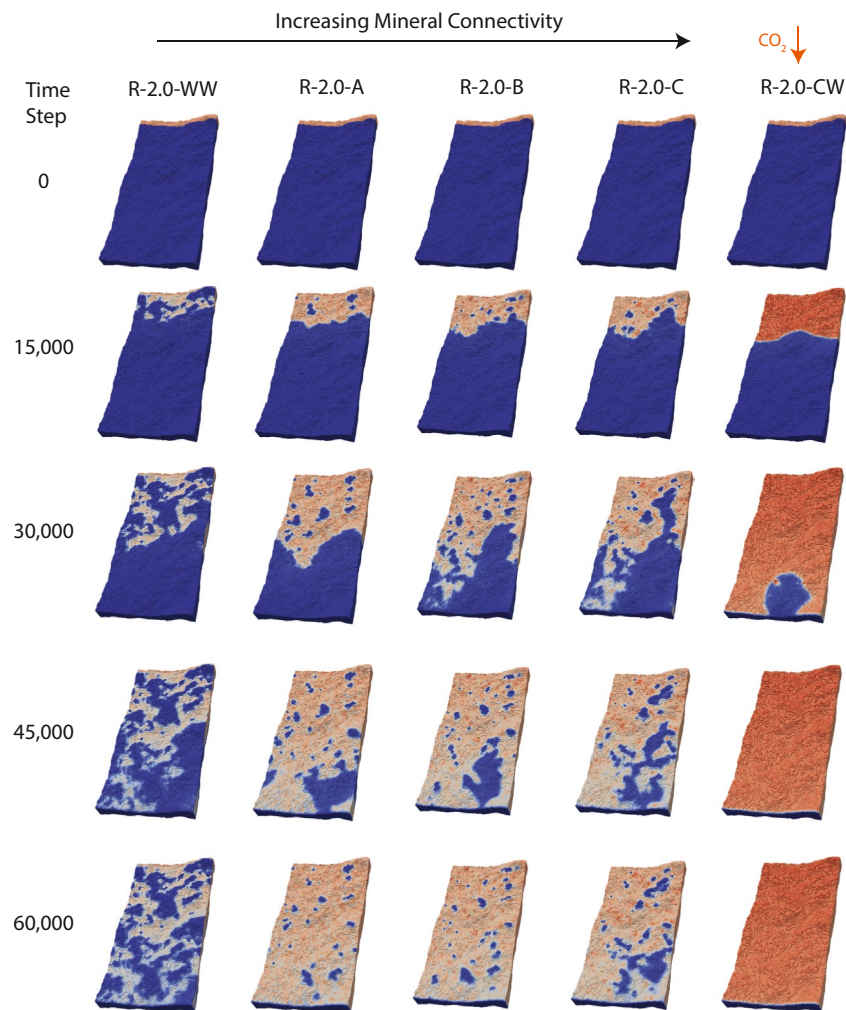
Figure 9. Evolution of scCO$_2$ plume during each regular aperture with fractal dimension of 2.0. In general, the scCO$_2$ reaches the outlet sooner, leaves less residual saturation, and provides greater sweep efficiency when the water-wet minerals are less connected.

permeability at lower capillary numbers and in the presence of strong wetting forces has many challenges. First, the capillary pressure scales along the scCO$_2$ front with the wetting force and fracture aperture. Second, the absence of a piston-like displacement means the front must be estimated. One technique is to conduct experiments using gravity drainage and to neglect capillary pressure (DiCarlo et al., 2000; Kianinejad et al., 2016). This technique can also be applied in the LBM by applying a body force to both fluids (Hao & Cheng, 2010; Ramstad et al., 2012). However, our models can also reflect the unsteady scCO$_2$ displacement process in the presence of capillary pressures.

To evaluate the unsteady permeability of our models, an interface detection algorithm was developed which measures the capillary pressure as well as the location of the interface with respect to the outlet (Appendix A). This allows for over a thousand individual pressure gradients along the front to be calculated at each time step. The algorithm avoids the low pressure environment caused by the spurious currents along the interface by advancing three lattice nodes away from the interface into the bulk scCO$_2$ phase. These measurements are averaged and along with the known average scCO$_2$ flux across the fracture are used to estimate the unsteady scCO$_2$ permeabilities through Darcy's law (Figure 12). Because the capillary pressure is maintained at the outlet, there is no sharp drop in pressure within the scCO$_2$ after breakthrough. Thus, these unsteady scCO$_2$ permeability curves were generated using an average pressure gradient across the
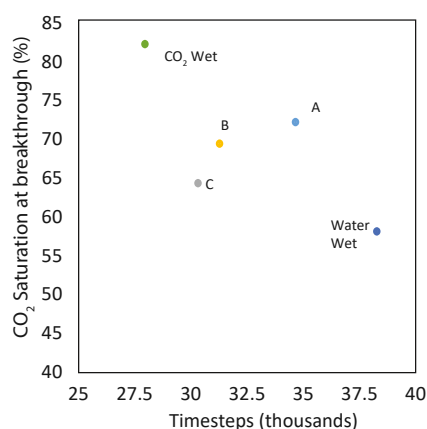
Figure 10. Average scCO$_2$ saturation and time step at breakthrough for wetting distributions applied to all fractures. The water-wet fractures take the longest to breakthrough and do so at the lowest saturation. The scCO$_2$ wet fracture has the highest scCO$_2$ saturation and breaks through the quickest. As the capillary pressure map becomes more correlated (A to C), breakthrough is reached more quickly and at a lower scCO$_2$ saturation.

average length of the scCO$_2$ plume with an average flux across the model. The method provides meaningful results which trend toward the steady-state permeability of each simulation.

At the same saturation, there is only a subtle decrease in unsteady permeability due to fracture roughness (Figure 12a). However, there is a notable difference between the scCO$_2$ wet and the water-wet case. The result that the wetting phase has higher permeability than the nonwetting phase at the same saturation is in contrast to the phenomena in porous media where the nonwetting phase occupies larger pores and thus has a higher relative permeability than the wetting phase at the same saturation. This effect in porous media is well known and has been recently noted in lattice Boltzmann simulations (Zhao et al., 2018). The difference in our simulations is likely due to the reduction of the effective aperture in the water-wet case caused by the residually saturated water pockets at the fracture surfaces. This trapping mechanism is absent in the scCO$_2$ wetting fractures, explaining their higher relative permeability, and also explains why roughness, which only increases the pockets of residual saturation in the water-wet case, has little effect on the relative permeability of the scCO$_2$ wet fractures.

In terms of the evolution of unsteady permeability with time (Figure 12b), a significant difference due to fracture roughness and wetting are both observed. The defending water phase is entirely and rapidly displaced during imbibition into the scCO$_2$-wet fractures. A decrease in the final permeability due to roughness in the scCO$_2$-wet fractures is akin to a reduction in permeability due to roughness as in the Reynolds lubrication model. A significant decrease in permeability is observed due to roughness during the drainage of the water-wet fractures. The change is greater than the imbibition cases due to the significantly increased residual saturation with roughness. The difference due to the scCO$_2$-wet and water-wet fracture surfaces is to be expected. The simulations predict that a wetting fluid will fully displace a nonwetting fluid and under these pressure conditions this will happen in approximately a third of the time it takes for the water-wet case to reach steady state.

The unsteady scCO$_2$ permeability evolution in the five different wetting models in the thin, regular, and wide fracture with fractal dimension of 2.0 is shown in Figure 13.

The evolution of unsteady scCO$_2$ permeability through time (Figure 13a) is bounded by the scCO$_2$-wet and water-wet fracture, with the heterogeneous wetting distributions falling in between. Wetting distribution A (with the least correlated capillary pressure field) has the highest permeabilities followed by B and C, although the difference is small. The effect of the wetting distributions on the fracture permeability increases as the fracture aperture widens (Figure 13a, panel #3). As the fracture aperture increases, it becomes easier for the scCO$_2$ to avoid the water-wetting minerals on the fracture surface. This promotes the first trapping mechanism, where the residually trapped water resides on the fracture surface.

On the basis of saturation (Figure 13b), each wetting distribution behaves similarly although the wetting and nonwetting simulations still bound the system. Overall these distributions are generally water-wet and would likely trend toward the fully scCO$_2$-wet case if the scCO$_2$-wetting fraction (kerogen) was increased.

To summarize this section, we found that during multiphase displacement in fractures when scCO$_2$ is the wetting phase it has a higher permeability than as the nonwetting phase at the same saturation. This is in direct contrast to porous media. We show that roughness significantly decreases permeability only in the nonwetting case due the increased residual saturation along the fracture walls which decreases the effective
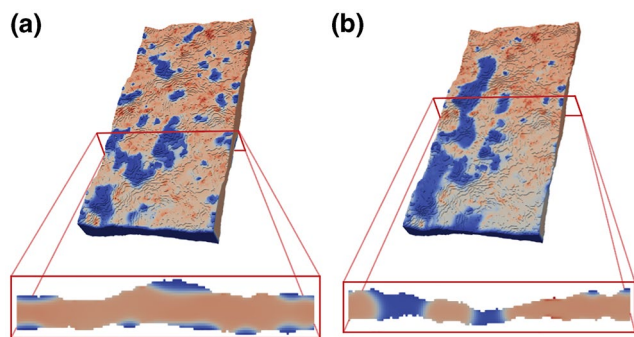

Figure 11. Trapping in a wide fracture simulation [(a) W-2.0-C] compared to a thin fracture [(b) T-2.0-C]. In the fractures with wide apertures, the residually trapped water is completely isolated to the fracture surfaces. In the thin fractures, areas of high and low capillary pressure cause large residually trapped water pockets which completely span the fracture aperture.
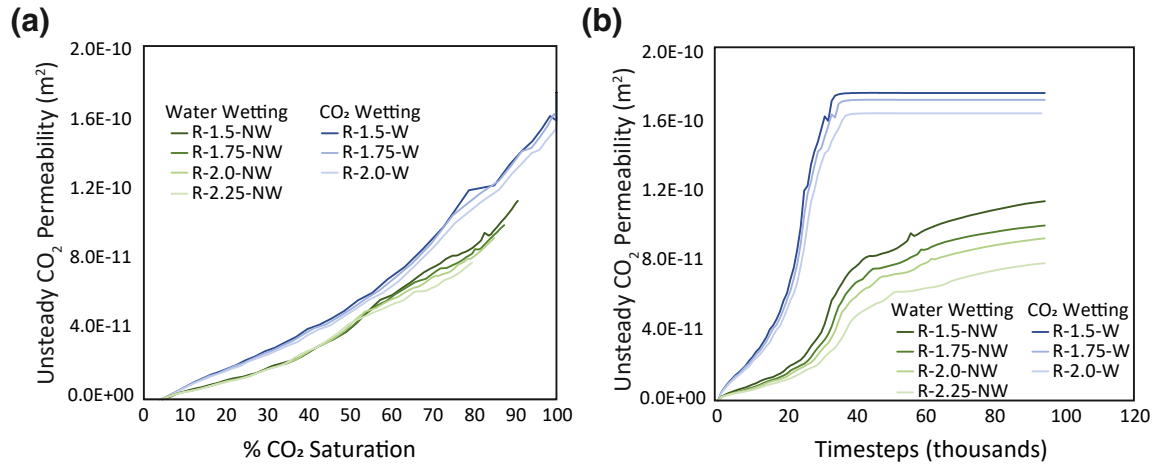
Figure 12. Effect of fracture correlation on the evolution of unsteady scCO$_2$ permeability in terms of (a) % scCO$_2$ saturation and (b) LBM time steps. Fracture simulation R-2.25-W was unstable and did not complete. LBM, lattice Boltzmann method.

aperture for flow. The wetting phase reaches steady state in ~1/3 the time it takes the nonwetting phase under the simulated pressure conditions due to negative capillary pressures. Finally, in heterogeneous wetting fractures, the unsteady permeability is inversely correlated to the correlation of the capillary pressure field; however, the differences are subtle.

3.3. Comparison to Relative Permeability Models

Three relative permeability models are commonly used in the literature. These techniques relate the saturation of each phase to the relative permeability of the fracture. The oldest and simplest relative permeability
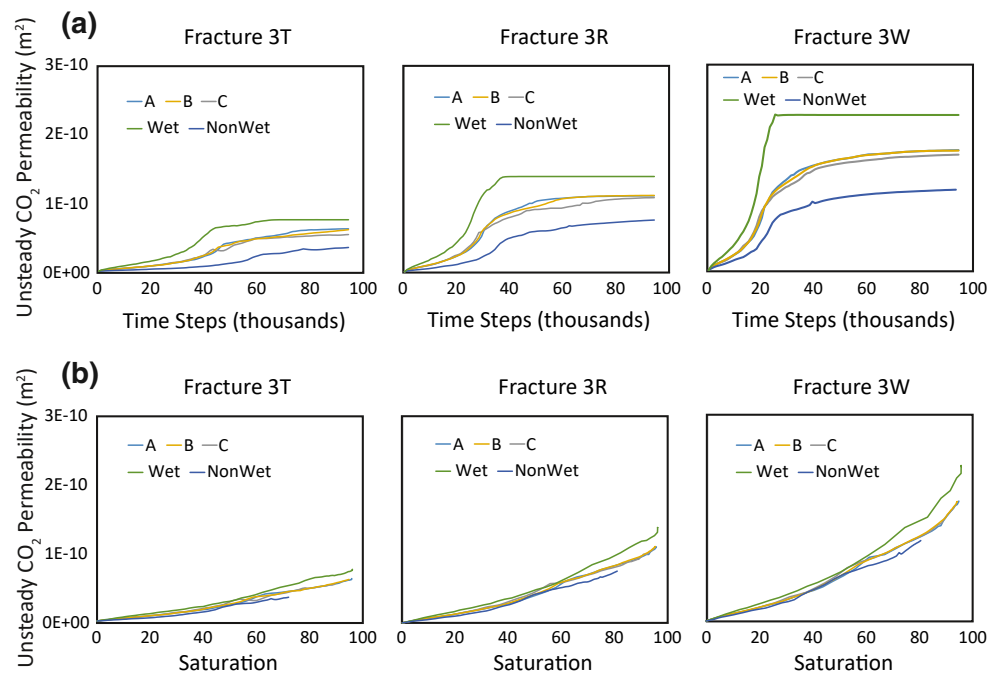

Figure 13. Unsteady permeability of each wetting distribution in the thin, regular, and wide fracture with fractal dimension 2.0: (a) in terms of model time step and (b) in terms of fracture scCO$_2$ saturation.
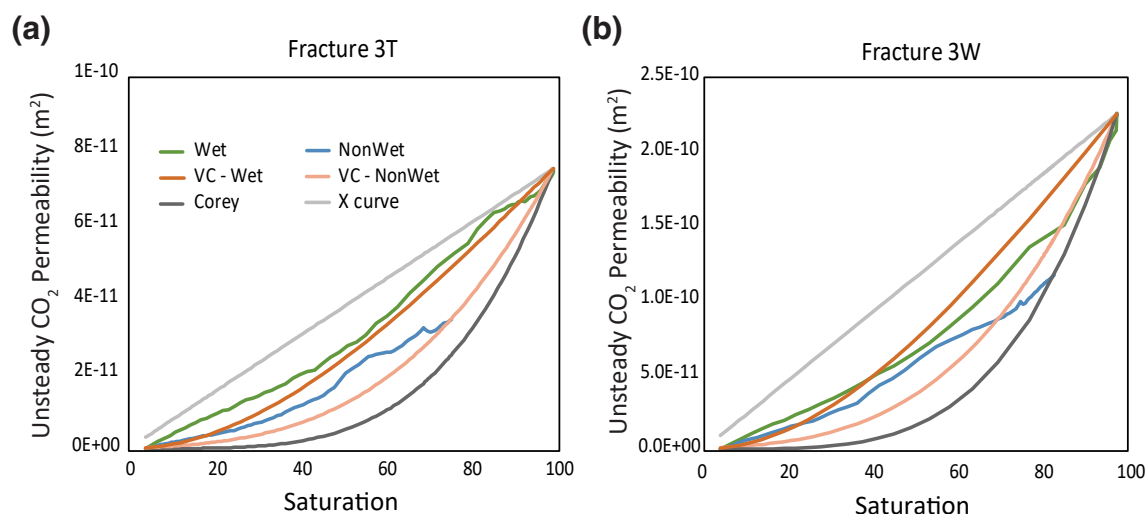
Figure 14. A comparison between the scCO$_2$ wetting and scCO$_2$ nonwetting permeability curves in the thin fracture #3 and the wide fracture #3. Overlain the simulated results are the X-model, Corey model, and viscous coupling (VC) model for relative permeability in fractures. The viscous coupling model most closely approximates the simulated results.

model, still used in many commercially available reservoir simulators, assumes a linear relationship between relative permeability and saturation (Shad & Gates, 2010). This model, known as the X-model due to the X-shape of the relative permeability curves, was first proposed by Romm (1966) and later validated experimentally (Pan et al., 1996). Corey (1994) proposed a nonlinear relationship between saturation and permeability that was also experimentally validated (Diomampo, 2001). Fourar and Lenormand (1998) proposed a method called viscous coupling (VC) which is based on the analytical solution for two-phase flow through a pipe with the assumption that one-phase wets the wall of the pipe while the other phase travels through the center.

As shown in Figure 14, our results generally fall between the Corey relative permeability curves and the simple linear X-model, and are in best agreement with the VC method. This is likely due to this method's ability to capture effects of the first trapping mechanism where the wetting fluid adheres to the fracture surfaces. The existence of a continuous wetting phase along the fracture face in the VC model is different than the discontinuous wetting films observed in our simulations but both reduce the effective aperture to some extent. The underestimation of the VC method is likely due to the assumption that the wetting phase completely wets the fracture surface where we observe only a partial wetting of the fracture surface. Conducting relative permeability experiments in fractures is difficult and controlling variables such as mean aperture, roughness, and wetting forces is almost impossible. Therefore, simulations such as those implemented here provide confidence in the VC method and support its incorporation into reservoir simulators.

3.4. Residual Saturation and Steady-State Relative Permeability

During immiscible displacement the residual saturation describes the amount of the defending phase which remains in the system at steady state. This value is important in many applications, but especially for predicting the amount of oil and gas which can be removed from a reservoir. The commonly employed X-curve model assumes that residual saturation in fractures is zero (Romm, 1966; Shad & Gates, 2010). However, our simulations predict residual saturation as high as 35% in our thin, rough, water-wet fracture (T-2.25-WW). This has important implications for predicting the production decline curves from hydraulically fractured unconventional reservoirs.

Santos et al. (2018) showed that residual saturation was linearly related to the standard deviation of aperture (σ_{ap}) in rough fractures at low capillary number. However, since each fracture set of the same fractal dimension (fractal dimension 1.5, 1.75, 2.0, 2.25) has the same σ_{ap} but different residual saturations and
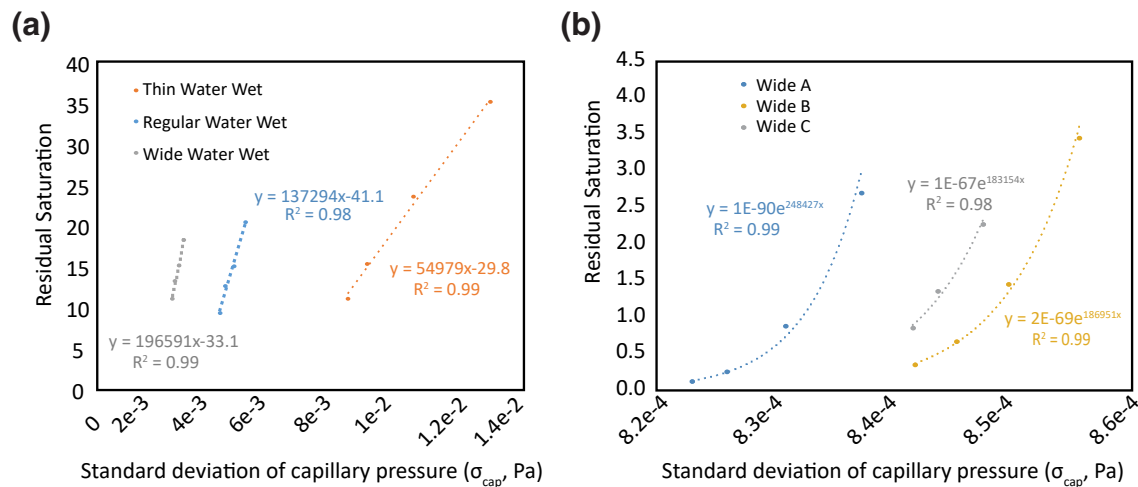
Figure 15. a) Linear correlation between saturation and σ_{cap} in water-wet fractures. (b) Exponential correlation between saturation and σ_{cap} in the wide fractures with wetting distribution A, B, and C. The simulation for fracture W-2.25-C was unstable resulting in only three simulations for wetting distribution C.

permeabilities, we instead explore a relationship between the standard deviation of capillary pressure (σ_{cap}) and saturation and permeability. The relationship between residual saturation and σ_{cap} is linear in the homogeneously water-wet fractures (Figure 15a). However, in the heterogeneously wet cases, the relationship is best described by an exponential (Figure 15b).

In the homogeneous case, the σ_{ap} and σ_{cap} are equivalent to each other (only different due to the multiplication of a constant). Thus, in the homogeneous case, the correlation to σ_{cap} is purely capturing the change in residual saturation as the aperture roughness is increased. In the heterogeneous cases, some areas, where residual saturation due to roughness may otherwise have occurred, does not because it encounters some sc-CO_2-wet minerals which interrupt the brine pockets allowing for displacement by scCO_2. As the roughness is increased the locations favorable to residual saturation become smaller and more plentiful, increasing the chance that they encounter only water-wet minerals. Thus, the roughness increases the amount of areas where water can be residually trapped in both the homogeneous wetting and heterogeneous wetting cases. However, the likelihood that they occur in locations of solely water-wet minerals is only increased in the heterogeneous cases.

The steady-state scCO_2 permeability for all the water-wet, scCO_2-wet, and heterogeneously wet distributions across all fractures is strongly correlated to σ_{cap} by a power-law relationship (Figure 16). From the relative permeability formulations of Fourar and Lenormand (1998) and Corey (1994), we expect a power-law relationship between saturation and permeability and we know that residual saturation is either linearly or power-law-related to σ_{cap} (Figure 15). In Figure 15, these relationships depend on the aperture (thin, regular, and wide) and wetting distribution (A, B, and C). In Figure 16, groupings associated with the thin, regular, and wide fractures can be seen. In the water-wet case (red circles), the greater effect of roughness on the fracture permeability can be seen by the separate correlation within each group. This greater effect is also apparent in Figure 12b. Despite this, the power-law correlation between permeability and σ_{cap} (Figure 16) exists across fracture aperture, roughness, and wetting distribution. Thus, σ_{cap} may be a better predictor of steady-state permeability than residual saturation. We hypothesize that the separate correlations for scCO_2 wetting, water-wetting, and wetting distributions A, B, and C observed in Figure 16 is related to the mean of capillary pressure field where the water-wetting and scCO_2 wetting mean capillary pressures are the same but of opposite sign, and wetting distributions A, B, and C each have approximately the same mean capillary pressure.

Measuring residual saturation in laboratory experiments is relatively straightforward in comparison to measuring the capillary pressure field and so the usefulness of this result may be called into question. However, our results show that the exact distribution of the capillary pressure field is considerably less important than the standard deviation when estimating steady-state relative permeability. We show that mineralogical
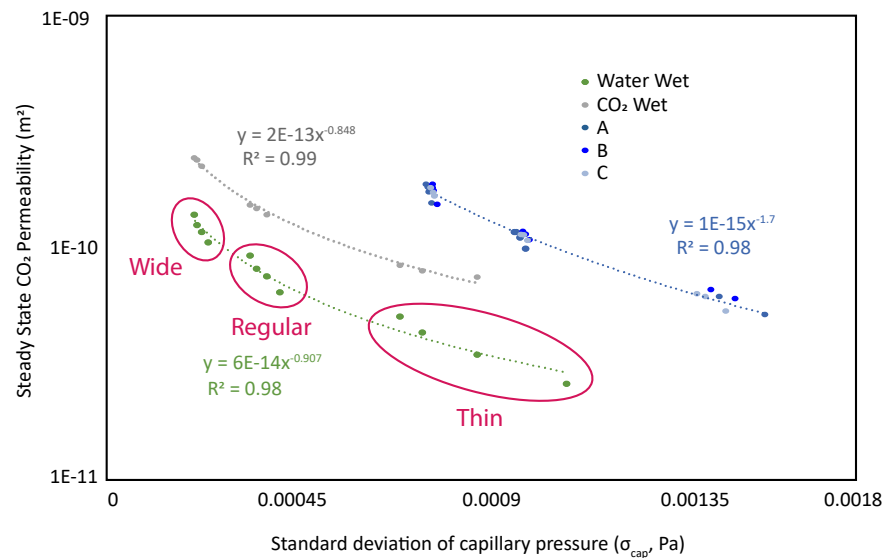
Figure 16. Exponential relationship between permeability and the standard deviation of capillary pressure across all simulations. The groupings highlighted by red circles are formed by the thin, regular, and wide apertures.

distributions A, B, and C, despite their differences, have a similar σ_{cap} and thus similar steady-state relative permeabilities. Thus, understanding the entire capillary pressure field is not necessary if assumptions about the aperture field and the mineralogical distributions effect on the σ_{cap} can be made.

4. Conclusions

We investigated the effect of heterogeneous wetting, informed from an organic shale, on multiphase displacement in fractures with varying roughness, and three different mean apertures. Using the *Taxila* LBM open source simulator (Coon et al., 2014; Porter et al., 2012), the roughness of the aperture field and the wetting distributions combine to form capillary pressure fields which control the displacement of water by $scCO_2$ and the evolution of the unsteady permeability as well as steady-state saturation and permeability. Two mechanisms of residual trapping in fractures were revealed in the simulations. The first occurs only in our thin aperture simulation and corresponds to a bypassing of the water within high capillary pressure zones by $scCO_2$; and the second occurs primarily in our regular and wide fracture apertures which exhibit a thin film of residually saturated water that occurs along the fracture surfaces corresponding to water-wet minerals. We show that the second type is significantly increased when the fracture aperture is increased.

An algorithm was developed to measure the position of the $scCO_2$ front and the capillary pressure across it. This allowed estimation of the unsteady $scCO_2$ permeability during the transient simulations and comparison to conventional relative permeability models from the literature. We found that the viscous coupling model of Fourar and Lenormand (1998), which accounts for a residually trapped phase along the fracture surface, best approximates our unsteady $scCO_2$ permeability curves. In contrast to porous media, we show that wetting phase has a higher permeability than the nonwetting phase at the same saturation. Analysis of the steady-state results shows a power-law relationship between the standard deviation of the capillary pressure field and the $scCO_2$ permeability of each fracture. This relationship persists across fracture roughness and mean aperture suggesting the capillary pressure field may be a better parameter to characterize relative permeability than saturation.

High-fidelity mechanistic simulations using high-performance computing like the ones presented in this paper provide insight on the dynamics of multiphase fluid flow and how microscale controls manifest as macroscale phenomena and parameters. Such simulations are not only useful for validating analytical and theoretical models and experimental results, they can be used to explore a broad space of numerous parameters and scenarios that are usually not covered by experiments and field observations.

Appendix A:

This appendix presents the python code used to detect the interface between CO_2 and brine within each fracture every 1,000 time steps. The code detects the interface where the LBM CO_2 density varies by greater than 0.2 across a range of 4 continuous lattice units. The program checks for walls and other interfaces to assure that interfaces near walls or interfaces within residual saturation "bubbles" are not used. The average length to the front, average CO_2 pressure along the front, and the CO_2 flux across the fracture are used to calculated the unsteady permeability of CO_2.

```python
import sys
import numpy as np
from sys import argv
sys.path.append ('/users/eguiltinan/petsc-3.6.4/bin')
import PetscBinaryIO
sys.path.append ('/users/eguiltinan/Taxila-LBM-master/src/testing')
import solution_reader3
# load a solution reader object which parses the input spec. Fracture files named 1,2,3 with wet-
ting A,B,C. eg: Fracture_1c. firstarg "1" secondarg "C." eg: Fracture_1C
firstarg = argv [1]
secondarg = argv [2]
sr = solution_reader3.SolutionReader ('/users/eguiltinan/Taxila-LBM-master/Fracture_'+
str (firstarg)+'/'+str (secondarg)+'/input_data')
#number of simulation steps
nsteps = 95
nx, ny, nz = 128, 256, 30
y = 150
ncells = nx * ny * nz
npoints = (nx + 1) * (ny + 1) * (nz + 1)
#Permeability(k) and flux (vel) will be recorded
k = np.zeros (nsteps)
vel = np.zeros (nsteps)
#yslice at which flux measurements will be taken
#chosen where near the front of the model where
#only CO2 exists.
yslice = 5
#load output files for each output at 1,000 time step intervals
#load, velocity, pressure, and density
files = range (nsteps)
for x in range (0,nsteps):

    if files [x] < 10:
        filename_v = '/u00'+str (files [x])+'.dat'
        filename_r = '/rho00'+str (files [x])+'.dat'
        filename_p = '/prs00'+str (files [x])+'.dat'
    if files [x] > 9:
        filename_v = '/u0'+str (files [x])+'.dat'
        filename_r = '/rho0'+str (files [x])+'.dat'
        filename_p = '/prs0' + str (files [x])+'.dat'
    if files [x] > 99:
        filename_v = '/u'+str (files [x])+'.dat'
        filename_r = '/rho'+str (files [x])+'.dat'
        filename_p = '/prs'+str (files [x])+'.dat'
    V = sr.loadVec (filename_v)
    rho = sr.loadVec (filename_r)
    pres = sr.loadVec (filename_p)
```

```
vx = np.random.rand (ncells).reshape ((nx, ny, nz), order = 'C')
vy = np.random.rand (ncells).reshape ((nx, ny, nz), order = 'C')
vz = np.random.rand (ncells).reshape ((nx, ny, nz), order = 'C')
density_water = np.random.rand (ncells).reshape ((nx, ny, nz), order = 'C')
density_co2 = np.random.rand (ncells).reshape ((nx, ny, nz), order = 'C')
velocity = np.random.rand (ncells).reshape ((nx, ny, nz), order = 'C')
vx [:,:,:] = v [:,:,:,0]
vy [:,:,:] = v [:,:,:,1]
vz [:,:,:] = v [:,:,:,2]
density_co2 [:,:,:] = rho [:,:,:,1]
density_water [:,:,:] = rho [:,:,:,0]
#rho1 and rho2 will measure the density difference across interface
    rho1 = 0
    rho2 = 0
    velocity_y = 0
    velocity_water = 0
    vy_count = 0
    vy_water_count = 0
#length, CO2 pressure at interface
    Length = np.zeros ((nx,nz))
    Pressure = np.zeros ((nz,nz))
    avg_Length = 0
    avg_Pres = 0
    avg_Pres_wat = 0
    for xcount in range (0,nz):
        for zcount in range (0,nz):
            for ycount in range (ny-5,5,-1):
                rho1 = density_co2 [xcount,ycount-2,zcount]
                rho2 = density_co2 [xcount, ycount+2,zcount]
# test for walls near the interface. Could do this with density as well.
                if pres [xcount, ycount+2,zcount]>0 and
                pres [xcount, ycount+1,zcount]>0 and
                pres [xcount, ycount,zcount]>0 and
                pres [xcount,ycount-1,zcount]>0 and
                pres [xcount,ycount-2,zcount]>0:
#if density difference is greater than 0.2 then its an interface
                        if rho1-rho2 > 0.20:
#now check if this is an isolated bubble by looking for a potential second interface
                            test = density_co2 [xcount, ycount:252,:]<0.75
                            if test.all ():
#if not an isolated bubble its an interface. Record pressure in CO2 at interface and length to
#interface
                                Length [xcount,zcount] = ycount
                                Pressure [xcount,zcount] = pres
                                [xcount,ycount-2,zcount]
                                break
#check for walls and then record the flux at each node and how many nodes are not walls at
#yslice
                        if vy [xcount, yslice,zcount]! = 0:
                            velocity_y = velocity_y + vy [xcount,yslice,zcount]
                            vy_count = vy_count + 1
    L_count = 0
    P_count = 0
    for xcount in range (0,nx):
```

```
for zcount in range (0,nz):
        if Length [xcount, zcount]>0:
                L_count = L_count + 1
                avg_Length = avg_Length + Length [xcount, zcount]
        if Pressure [xcount, zcount]>0:
                P_count = P_count +1
                avg_Pres = avg_Pres + Pressure [xcount, zcount]
    print "Average Length to interface = ," avg_Length/L_count
    print "Average CO2 Pressure at interface = ," avg_Pres/P_count
    print "Average total flux = ," velocity_y/vy_count
    vel [x] = velocity_y/vy_count
    k[x] = 0.0833*(velocity_y/vy_count)*(avg_Length/L_count)/(0.38-avg_Pres/P_count)
    print "Unsteady CO2 k," k [x]
    np.savetxt ('./Unsteady_Kr/Unsteady_CO2_'+str (firstarg)+'_'+str (secondarg)+'.txt', k, delimiter = 'b')
    np.savetxt    ('./Unsteady_velocity/Unsteady_vel_'+str    (firstarg)+'_'+str    (secondarg)+'.txt',    vel,
delimiter = 'b')
```

References

Aidun, C. K., & Clausen, J. R. (2010). Lattice-Boltzmann method for complex flows. *Annual Review of Fluid Mechanics*, *42*(1), 439–472. https://www.annualreviews.org/doi/abs/10.1146/annurev-fluid-121108-145519

Al-Raoush, R. I. (2009). Impact of wettability on pore-scale characteristics of residual nonaqueous phase liquids. *Environmental Science and Technology*, *43*(13), 4796–4801.

An, S., Hasan, S., Erfani, H., Babaei, M., & Niasar, V. (2020). Unravelling effects of the pore-size correlation length on the two-phase flow and solute transport properties: GPU-based pore-network modeling. *Water Resources Research*, *56*, e2020WR027403. https://doi.org/10.1029/2020WR027403

Armstrong, R. T., Porter, M. L., & Wildenschild, D. (2012). Linking pore-scale interfacial curvature to column-scale capillary pressure. *Advances in Water Resources*, *46*, 55–62.

Benson, S., Cook, P., Anderson, J., Bachu, S., Nimir, H., Basu, B., et al. (2005). Underground geological storage. IPCC Special Report on Carbon Dioxide Capture and Storage (pp. 195–265). Cambridge: Cambridge University Press.

Blunt, M. J., Bijeljic, B., Dong, H., Gharbi, O., Iglauer, S., Mostaghimi, P., et al. (2013). Pore-scale imaging and modelling. *Advances in Water Resources*, *51*, 197–216. http://www.sciencedirect.com/science/article/pii/S0309170812000528

Buckley, S. E., & Leverett, M. C. (1942). Mechanism of fluid displacement in sands. *Transactions of the AIME*, *146*, 107–116. https://doi.org/10.2118/942107-G

Chaudhary, K., Bayani Cardenas, M., Wolfe, W. W., Maisano, J. A., Ketcham, R. A., & Bennett, P. C. (2013). Pore-scale trapping of super-critical CO_2 and the role of grain wettability and shape. *Geophysical Research Letters*, *40*, 3878–3882. http://dx.doi.org/10.1002/grl.50658

Chen, S., & Doolen, G. D. (1998). Lattice Boltzmann method for fluid flows. *Annual Review of Fluid Mechanics*, *30*(1), 329–364. https://www.annualreviews.org/doi/abs/10.1146/annurev.fluid.30.1.329

Chen, Y. F., Fang, S., Wu, D. S., & Hu, R. (2017). Visualizing and quantifying the crossover from capillary fingering to viscous fingering in a rough fracture. *Water Resources Research*, *53*, 7756–7772. https://doi.org/10.1002/2017WR021051

Chen, L., Kang, Q., Mu, Y., He, Y.-L., & Tao, W.-Q. (2014). A critical review of the pseudopotential multiphase lattice Boltzmann model: Methods and applications. *International Journal of Heat and Mass Transfer*, *76*, 210–236.

Coon, E. T., Porter, M. L., & Kang, Q. (2014). Taxila LBM: A parallel, modular lattice Boltzmann framework for simulating pore-scale flow in porous media. *Computational Geosciences*, *18*(1), 17–27. https://doi.org/10.1007/s10596-013-9379-6

Corey, A. T. (1994). *Mechanics of immiscible fluids in porous media*, Water Resources Publication.

Culligan, K. A., Wildenschild, D., Christensen, B. S. B., Gray, W. G., & Rivers, M. L. (2006). Pore-scale characteristics of multiphase flow in porous media: A comparison of air-water and oil-water experiments. *Advances in Water Resources*, *29*(2), 227–238.

Dehghanpour, H., Aminzadeh, B., Mirzaei, M., & DiCarlo, D. A. (2011). Flow coupling during three-phase gravity drainage. *Physical Review E*, *83*(6), 065302.

DiCarlo, D. A., Akshay, S., & Blunt, M. J. (2000). Three-phase relative permeability of water-wet, oil-wet, and mixed-wet sandpacks. *SPE Journal*, *5*(1), 82–91. https://doi.org/10.2118/60767-PA

Diomampo, G. (2001). *Relative Permeability Through Fractures*, Stanford, CA: Stanford University. https://doi.org/10.2172/896520

Dou, Z., Zhou, Z., & Sleep, B. E. (2013). Influence of wettability on interfacial area during immiscible liquid invasion into a 3D self-affine rough fracture: Lattice Boltzmann simulations. *Advances in Water Resources*, *61*, 1–11. http://www.sciencedirect.com/science/article/pii/S0309170813001462

Eker, E., & Akin, S. (2006). Lattice Boltzmann simulation of fluid flow in synthetic fractures. *Transport in Porous Media*, *65*(3), 363–384. https://doi.org/10.1007/s11242-005-6085-4

Fourar, M., & Lenormand, R. (1998). *A viscous coupling model for relative permeabilities in fractures*, Paper presented at the SPE Annual Technical Conference and Exhibition. Society of Petroleum Engineers. https://doi.org/10.2118/49006-MS

Gale, J. F. W., Reed, R. M., & Holder, J. (2007). Natural fractures in the Barnett Shale and their importance for hydraulic fracture treatments. *AAPG Bulletin*, *91*(4), 603–622.

Gerke, K. M., Karsanina, M. V., & Mallants, D. (2015). Universal stochastic multiscale image fusion: An example application for shale rock. *Scientific Reports*, *5*, 15880. http://dx.doi.org/10.1038/srep15880

Glover, P. W. J., Matsuki, K., Hikima, R., & Hayashi, K. (1998a). Fluid flow in synthetic rough fractures and application to the Hachimantai geothermal hot dry rock test site. *Journal of Geophysical Research*, *103*(B5), 9621–9635. https://doi.org/10.1029/97JB01613

Glover, P. W. J., Matsuki, K., Hikima, R., & Hayashi, K. (1998b). Synthetic rough fractures in rocks. *Journal of Geophysical Research*, *103*(B5), 9609–9620. https://doi.org/10.1029/97JB02836

Guiltinan, E. J., Cardenas, M. B., Bennett, P. C., Zhang, T., & Espinoza, D. N. (2017). The effect of organic matter and thermal maturity on the wettability of supercritical CO_2 on organic shales. *International Journal of Greenhouse Gas Control*, *65*, 15–22.

Hao, L., & Cheng, P. (2010). Pore-scale simulations on relative permeabilities of porous media by lattice Boltzmann method. *International Journal of Heat and Mass Transfer*, *53*(9–10), 1908–1913.

Hu, R., Wan, J., Kim, Y., & Tokunaga, T. K. (2017). Wettability effects on supercritical CO_2–brine immiscible displacement during drainage: Pore-scale observation and 3D simulation. *International Journal of Greenhouse Gas Control*, *60*, 129–139. http://www.sciencedirect.com/science/article/pii/S1750583616306715

Johnson, E. F., Bossler, D. P., & Bossler, V. O. N. (1959). Calculation of relative permeability from displacement experiments. *Transactions of the AIME*, *216*, 370–372. https://doi.org/10.2118/1023-G

Ju, Y., Zhang, Q., Zheng, J., Chang, C., & Xie, H. (2017). Fractal model and lattice Boltzmann method for characterization of non-Darcy flow in rough fractures. *Scientific Reports*, *7*, 41380. http://dx.doi.org/10.1038/srep41380

Kianinejad, A., Chen, X., & DiCarlo, D. A. (2016). Direct measurement of relative permeability in rocks from unsteady-state saturation profiles. *Advances in Water Resources*, *94*, 1–10. http://www.sciencedirect.com/science/article/pii/S030917081630121X

Kim, I., Lindquist, W., & Durham, W. (2003). Fracture flow simulation using a finite-difference lattice Boltzmann method. *Physical Review E*, *67*(4), 046708.

Landry, C. J., Karpyn, Z. T., & Ayala, O. (2014). Pore-scale lattice Boltzmann modeling and 4D X-ray computed microtomography imaging of fracture-matrix fluid transfer. *Transport in Porous Media*, *103*(3), 449–468. http://dx.doi.org/10.1007/s11242-014-0311-x

Laplace, P. S. (1799). *Traité de mécanique céleste* (Vol. 1). Paris, France: Imprimerie Crapelet.

Lemmon, E. W., McLinden, M. O., & Friend, D. G. (2020). Thermophysical properties of fluid systems. In P. J. Linstrom & W. G. Mallard (Eds.), *NIST Chemistry WebBook, NIST Standard Reference Database Number 69*.Gaithersburg, MD: National Institute of Standards and Technology. https://doi.org/10.18434/T4D303

Li, Q., Luo, K. H., Kang, Q., He, Y., Chen, Q., & Liu, Q. (2016). Lattice Boltzmann methods for multiphase flow and phase-change heat transfer. *Progress in Energy and Combustion Science*, *52*, 62–105.

Liu, F., Lu, P., Zhu, C., & Xiao, Y. (2011). Coupled reactive flow and transport modeling of CO_2 sequestration in the Mt. Simon sandstone formation, Midwest U.S.A. *International Journal of Greenhouse Gas Control*, *5*, 294–307.

Meakin, P., & Tartakovsky, A. M. (2009). Modeling and simulation of pore-scale multiphase fluid flow and reactive transport in fractured and porous media. *Reviews of Geophysics*, *47*, RG3002. https://doi.org/10.1029/2008RG000263

Naylor, P., Sargent, N. C., Crosbie, A. J., Tilsed, A. P., & Goodyear, S. G. (1996). Gravity drainage during gas injection. *Petroleum Geoscience*, *2*(1), 69–74.

Nourgaliev, R. R., Dinh, T. N., Theofanous, T. G., & Joseph, D. (2003). The lattice Boltzmann equation method: Theoretical interpretation, numerics and implications. *International Journal of Multiphase Flow*, *29*(1), 117–169. http://www.sciencedirect.com/science/article/pii/S0301932202001088

Ogilvie, S. R., Isakov, E., & Glover, P. W. J. (2006). Fluid flow through rough fractures in rocks. II: A new matching model for rough rock fractures. *Earth and Planetary Science Letters*, *241*(3), 454–465. http://www.sciencedirect.com/science/article/pii/S0012821X05008174

Pacala, S., & Socolow, R. (2004). Stabilization wedges: Solving the climate problem for the next 50 years with current technologies. *Science*, *305*(5686), 968–972. http://science.sciencemag.org/content/sci/305/5686/968.full.pdf

Pan, X., Wong, R., & Maini, B. (1996). *Steady state two-phase in a smooth parallel fracture*. Paper presented at the Annual Technical Meeting, Calgary, Alberta. Petroleum Society of Canada. https://doi.org/10.2118/96-39

Peters, E. J. (2012). *Advanced Petrophysics: Dispersion, Interfacial Phenomena* (Vol. 2). Austin, TX: Live Oak Book Company.

Porter, M. L., Coon, E. T., Kang, Q., Moulton, J. D., & Carey, J. W. (2012). Multicomponent interparticle-potential lattice Boltzmann model for fluids with large viscosity ratios. *Physical Review E*, *86*(3), 036701. https://link.aps.org/doi/10.1103/PhysRevE.86.036701

Ramstad, T., Idowu, N., Nardi, C., & Øren, P.-E. (2012). Relative permeability calculations from two-phase flow simulations directly on digital images of porous rocks. *Transport in Porous Media*, *94*(2), 487–504. https://doi.org/10.1007/s11242-011-9877-8

Remy, N., Boucher, A., & Wu, J. (2009). *Applied Geostatistics with SGeMS: A User's Guide*. Cambridge: Cambridge University Press.

Renshaw, C. E. (1995). On the relationship between mechanical and hydraulic apertures in rough-walled fractures. *Journal of Geophysical Research*, *100*(B12), 24629–24636. https://agupubs.onlinelibrary.wiley.com/doi/abs/10.1029/95JB02159

Romm, E. (1966). *Flow Characteristics of Fractured Rocks*. Moscow: Nedra.

Sahni, A., Burger, J., & Blunt, M. (1998). *Measurement of three phase relative permeability during gravity drainage using CT*. Paper presented at the SPE/DOE Improved Oil Recovery Symposium, Tulsa, Oklahoma. Society of Petroleum Engineers. https://doi.org/10.2118/39655-MS

Santos, J. E., Prodanovic, M., Landry, C. J., & Jo, H. (2018). Determining the impact of mineralogy composition for multiphase flow through hydraulically induced fractures. In *Unconventional Resources Technology Conference* (pp. 232542–252556). Houston, TX: Society of Exploration Geophysicists, American Association of Petroleum Geologists, Society of Petroleum Engineers.

Shad, S., & Gates, I. D. (2010). Multiphase flow in fractures: Co-current and counter-current flow in a fracture. *Journal of Canadian Petroleum Technology*, *49*(2), 48–55. https://doi.org/10.2118/133205-PA

Shan, X., & Chen, H. (1993). Lattice Boltzmann model for simulating flows with multiple phases and components. *Physical Review E*, *47*(3), 1815–1819. https://link.aps.org/doi/10.1103/PhysRevE.47.1815

Shan, X., & Chen, H. (1994). Simulation of nonideal gases and liquid-gas phase transitions by the lattice Boltzmann equation. *Physical Review E*, *49*(4), 2941–2948. https://link.aps.org/doi/10.1103/PhysRevE.49.2941

Sukop, M., & Thorne, D. T., Jr. (2006). *Lattice Boltzmann modeling. An introduction for geoscientists and engineers*, Berlin, Germany: Springer.

Vogler, D., Settgast, R. R., Annavarapu, C., Madonna, C., Bayer, P., & Amann, F. (2018). Experiments and simulations of fully hydro-mechanically coupled response of rough fractures exposed to high-pressure fluid injection. *Journal of Geophysical Research: Solid Earth*, *123*, 1186–1200. https://agupubs.onlinelibrary.wiley.com/doi/abs/10.1002/2017JB015057

Wang, L., & Cardenas, M. B. (2014). Non-Fickian transport through two-dimensional rough fractures: Assessment and prediction. *Water Resources Research*, *50*, 871–884. https://agupubs.onlinelibrary.wiley.com/doi/abs/10.1002/2013WR014459

Wang, L., Cardenas, M. B., Slottke, D. T., Ketcham, R. A., & Sharp, J. M. (2015). Modification of the local cubic law of fracture flow for weak inertia, tortuosity, and roughness. *Water Resources Research*, *51*, 2064–2080. https://agupubs.onlinelibrary.wiley.com/doi/abs/10.1002/2014WR015815

Yang, Z., Neuweiler, I., Méheust, Y., Fagerlund, F., & Niemi, A. (2016). Fluid trapping during capillary displacement in fractures. *Advances in Water Resources*, *95*, 264–275.

Young, T. (1805). III. An essay on the cohesion of fluids. *Philosophical Transactions of the Royal Society of London*, *95*, 65–87.

Yu, Z., Yang, H., & Fan, L.-S. (2011). Numerical simulation of bubble interactions using an adaptive lattice Boltzmann method. *Chemical Engineering Science*, *66*(14), 3441–3451. http://www.sciencedirect.com/science/article/pii/S0009250911000297

Zhang, J. (2011). Lattice Boltzmann method for microfluidics: Models and applications. *Microfluidics and Nanofluidics*, *10*(1), 1–28. https://doi.org/10.1007/s10404-010-0624-1

Zhao, B., MacMinn, C. W., Primkulov, B. K., Chen, Y., Valocchi, A. J., Zhao, J., et al. (2019). Comprehensive comparison of pore-scale models for multiphase flow in porous media. *Proceedings of the National Academy of Sciences of the United States of America*, *116*, 13799–13806.

Zhao, J., Kang, Q., Yao, J., Viswanathan, H., Pawar, R., Zhang, L., & Sun, H. (2018). The effect of wettability heterogeneity on relative permeability of two-phase flow in porous media: A lattice Boltzmann study. *Water Resources Research*, *54*, 1295–1311. https://agupubs.onlinelibrary.wiley.com/doi/abs/10.1002/2017WR021443